



HAL
open science

Iterative tomographic reconstruction with TV prior for low-dose CBCT dental imaging

Louise Friot–Giroux, Françoise Peyrin, Voichita Maxim

► **To cite this version:**

Louise Friot–Giroux, Françoise Peyrin, Voichita Maxim. Iterative tomographic reconstruction with TV prior for low-dose CBCT dental imaging. *Physics in Medicine and Biology*, 2022, 67 (20), pp.205010. 10.1088/1361-6560/ac950c . hal-04224784

HAL Id: hal-04224784

<https://cnrs.hal.science/hal-04224784v1>

Submitted on 13 Nov 2024

HAL is a multi-disciplinary open access archive for the deposit and dissemination of scientific research documents, whether they are published or not. The documents may come from teaching and research institutions in France or abroad, or from public or private research centers.

L'archive ouverte pluridisciplinaire **HAL**, est destinée au dépôt et à la diffusion de documents scientifiques de niveau recherche, publiés ou non, émanant des établissements d'enseignement et de recherche français ou étrangers, des laboratoires publics ou privés.

Iterative tomographic reconstruction with TV prior for low-dose CBCT dental imaging

Louise Friot--Giroux, Françoise Peyrin, Voichita Maxim

Univ Lyon, INSA-Lyon, Université Claude Bernard Lyon 1, CNRS, Inserm, CREATIS UMR 5220, U1294, F-69100, LYON, France

E-mail: louise.friot--giroux@creatis.insa-lyon.fr

September 2022

Abstract.

Objective Cone-Beam Computed Tomography is becoming more and more popular in applications such as 3D dental imaging. Iterative methods compared to the standard Feldkamp algorithm have shown improvements in image quality of reconstruction of low-dose acquired data despite their long computing time. An interesting aspect of iterative methods is their ability to include prior information such as sparsity-constraint. While a large panel of optimization algorithms along with their adaptation to tomographic problems are available, they are mainly studied on 2D parallel or fan-beam data. The issues raised by 3D CBCT and moreover by truncated projections are still poorly understood.

Approach We compare different carefully designed optimization schemes in the context of realistic 3D dental imaging. Besides some known algorithms, SIRT-TV and MLEM, we investigate the primal-dual hybrid gradient (PDHG) approach and a newly proposed MLEM-TV optimizer. The last one is alternating EM steps and TV-denoising, combination not yet investigated for CBCT. Experiments are performed on both simulated data from a 3D jaw phantom and data acquired with a dental clinical scanner.

Main results With some adaptations to the specificities of CBCT operators, PDHG and MLEM-TV algorithms provide the best reconstruction quality. These results were obtained by comparing the full-dose image with a low-dose image and an ultra low-dose image.

Significance The convergence speed of the original iterative methods is hampered by the conical geometry and significantly reduced compared to parallel geometries. We promote the pre-conditioned version of PDHG and we propose a pre-conditioned version of the MLEM-TV algorithm. To the best of our knowledge, this is the first time PDHG and convergent MLEM-TV algorithms are evaluated on experimental dental CBCT data, where constraints such as projection truncation and presence of metal have to be jointly overcome.

Keywords: CBCT, Dental Imaging, Iterative Reconstruction

Submitted to: *Phys. Med. Biol.*

1. Introduction

Cone-Beam Computed Tomography (CBCT) is a 3D X-ray imaging technique where an object is reconstructed from a set of its 2D cone-beam projections acquired on 2D detectors. In dental imaging, CBCT enables to reduce the dose sent to the patient and to reduce the acquisition time compared to conventional CT scanners, making the use of such scanners much more frequent [Liang et al., 2010]. However, as in other CT-based techniques, a trend in CBCT imaging is to reduce the ionizing radiation dose depositions, that come with subsequent undesirable effects for patients.

Standard image reconstruction in CBCT is generally performed using analytical methods, providing the reconstructed image in a negligible amount of time. The FDK algorithm [Feldkamp et al., 1984], an heuristic extension of the 2D Filtered Back Projection (FBP) algorithm, is the most popular algorithm in CBCT despite the apparition of so-called cone-beam artifact when associated to a circular trajectory of the source. In addition, analytical methods relying on a continuous formulation of the direct problem, are quite sensitive to discretization conditions, and in particular to the number of projections. This therefore leads to reconstructed images likely to be affected by noise and various artifacts in low-dose conditions. Nevertheless, the FDK algorithm is still the most commonly employed method in dental CBCT, either used alone in the case of high-dose [Baba et al., 2004] or associated to pre and/or post-processing to reduce some artifacts (metal in [Ibraheem et al., 2012], beam hardening and noise in [Bayaraa et al., 2020]) and to improve the image quality.

In this context, iterative reconstruction methods are a flexible alternative to analytical methods. Basic iterative CT reconstruction methods include for instance, the conventional Algebraic Reconstruction Technique (ART) [Gordon et al., 1970], which is based on the Kaczmarz method and works ray by ray, or the Simultaneous Iterative Reconstruction Technique (SIRT) [Gilbert, 1972] and Simultaneous Algebraic Reconstruction Technique (SART) [Andersen and Kak, 1984] algorithms, that work on the whole volume and are more robust than ART. Statistical methods allow the inclusion of a priori information on the photon distribution statistics. Among them, the Maximum Likelihood Expectation Maximization (MLEM) algorithm [Shepp and Vardi, 1982] used in emission tomography has been adapted to transmission tomography in several works [Lange et al., 1984, Vardi et al., 1985]. To speed up the reconstruction, the data can be divided into subsets leading to the so-called OSEM methods [Hudson and Larkin, 1994, Mtanglos et al., 1995].

However, in order to avoid the semi-convergent nature of most of these algorithms, the state-of-the-art solution is to include regularization in the form of prior information about the volume to be reconstructed, leading to the so-called model-based methods. Regularizers based on the l_2 -norm have been widely used in the past. Sparsity-based regularizers such as total variation (TV), introduced for image denoising by Rudin, Osher and Fatemi [Rudin et al., 1992] have demonstrated excellent results in many applications, including tomographic reconstruction [Sidky et al., 2006,

Banjak et al., 2018]. In [Kolehmainen et al., 2003], the authors applied statistical iterative methods to dental CT-scan, with a TV regularization. Some iterative algorithms already implemented on commercialized CT devices have shown very good results in terms of noise and artifacts suppression [Widmann et al., 2017, Widmann and Asma'a, 2018]. However, they still remain barely used in practice for dental CBCT [Kaasalainen et al., 2021].

Data-driven methods based on Deep Learning (DL) methods are also attractive for CT reconstruction problem. Various schemes have been proposed, most of the time based on post-processing and correction strategies to enhance a FDK reconstruction [Jin et al., 2017, Park and Ye, 2020]. Another strategy consists in the direct resolution of the inverse problem as in [Li et al., 2019], where the network is conceived to transform sinogram data into images, or in [Adler and Öktem, 2018] where the physical model of the acquisition is included. Although DL methods can give impressive results on simulations, they usually need extensive training on representative datasets and require large datasets, especially in 3D CBCT. Moreover, some uncertainties subsist about their reliability for medical applications.

While a large panel of iterative algorithms are available, they have been mostly evaluated on 2D parallel or fan-beam data and rarely on 3D cone-beam projections. The specific geometry of CBCT coupled with dental imaging brings challenges in the reconstruction process that are not encountered in parallel beam models. On the one hand, despite hardware progresses made with the development of Graphic Processing Units (GPUs), computing resources are still an issue for iterative methods, especially in 3D CBCT. Finding a fast converging iterative scheme among the panel of available algorithms is thus relevant. On the other hand, there are also practical issues for applications to dental imaging like the problem of truncated projections since the detector size is smaller than the patient's head. Truncated projections lead to artifacts in the reconstructed image, creating bright bands that decrease the image quality and prevent a correct diagnostic. Several methods that mitigate truncation effects have been developed. Schemes extrapolating the projections, like including symmetric mirroring [Ohnesorge et al., 2000] or water cylinder fitting [Hsieh et al., 2004] have been proposed for analytical reconstructions. For iterative reconstructions, the most common strategy consists in increasing the reconstruction field of view [Dang et al., 2016, Aootaphao et al., 2021]. Hence, the information issued from the truncated part is sent to the space provided by this extension of the matrix volume.

In this paper, we compare different iterative algorithms with TV regularization in order to reconstruct volumes from truncated and low-dose projections. We select some relevant algorithms from different families encountered in the literature and we identify their strengths and weaknesses, as well as ways to overcome the last ones. To the best of our knowledge, these methods have never been applied to dental CBCT data and some of them required adjustments. Although our comparison is not exhaustive, it should give a fair survey of the potential of such methods.

The SIRT-TV method from [Banjak et al., 2018] consists in alternating SIRT and TV denoising steps. The algorithm is accelerated with a FISTA (Fast Iterative Shrinkage Thresholding Algorithm) step [Beck and Teboulle, 2009a]. An important objective being dose reduction, along with SIRT which is representative of algebraic methods and is widely used in non-medical applications where computing time is less an issue, we also consider two algorithms designed for Poisson distributed data. In this case, the cost function is composed of a Kullback-Leibler data fidelity term and a TV semi-norm. One of them is a Primal Dual Hybrid Gradient (PDHG) scheme [Chambolle and Pock, 2011] particularized for tomographic reconstruction in [Sidky et al., 2012]. As in [Sidky et al., 2012], we use the preconditioned version of PDHG from [Pock and Chambolle, 2011] that provides faster convergence and is better adapted to complex projector operators such as the one from CBCT. Following [Sidky et al., 2012], we will call this algorithm KL-TV. As in SIRT-TV, a step-alternating strategy can also be used for Poisson data [Sawatzky et al., 2008, Yan et al., 2011]. These methods are a step forward compared to the Maximum A Posteriori (MAP) approach introduced in [Green, 1990] which requires a very small regularization parameter, tends to blur the reconstruction and leads to numerical instabilities [Panin et al., 1999, Persson et al., 2001]. We chose to use the step-alternating algorithm from [Maxim et al., 2018] which was proven to be convergent. The TV denoising is solved using the convex-duality principle of Fenchel-Rockafellar. To accelerate the denoising step and following [Pock and Chambolle, 2011], we also introduce a preconditioning that relies on the projection matrix. This algorithm will be referred as MLEM-TV.

In this work, since we focus on the suitability of these iterative reconstruction methods for low-dose dental CBCT imaging, we detail how to adapt them to the cone-beam geometry and to reconstruct from truncated projections. Our objectives are to: 1) evaluate the quality of the produced images; 2) evaluate the computing time and computing resources; 3) investigate potential of improvement. These carefully designed TV-based optimization schemes are then evaluated on an experimental CBCT acquisition.

This paper is organized as follows. In the second section, we introduce the notations and the basics of tomographic reconstruction. Then, we derive the framework of our method: the algorithms used are detailed in the second section, and the description of the data used for evaluation is given in the third section. In the fourth section, we present the results of the algorithms on phantom data to evaluate their robustness to noisy data, and, finally on experimental dental data. In the fifth section, we discuss the obtained results. Conclusions and perspectives are given in the last section.

2. Methods

2.1. Tomographic reconstruction problem

After traversing an attenuating medium, the intensity \mathcal{I} of a X-ray beam having initial intensity \mathcal{I}_0 is modeled by the Beer-Lambert law. For a volume f divided in $J = M \times N \times N$ voxels indexed by $j = 1, \dots, J$, the Beer-Lambert law writes:

$$\mathcal{I} = \mathcal{I}_0 \exp\left(-\sum_j L_j f_j\right), \quad (1)$$

where f_j is the linear attenuation coefficient of the j^{th} voxel and L_j is the length of the intersection between the beam and the voxel. The volume f can be determined when a sufficient number of beams indexed on $i = 1, \dots, I$, are sent through the object. We denote hereafter a_{ij} the intersection length of the i th beam and the j th voxel, previously denoted L_j in (1). The value:

$$p_i = -\log\left(\frac{\mathcal{I}}{\mathcal{I}_0}\right) = \sum_j a_{ij} f_j \quad (2)$$

is the linear projection of the volume following the i th beam direction. The vector of projections will be noted hereafter p and indexed on $i = 1, \dots, I$. The tomographic problem is finally modelled by the following linear equation:

$$Af = p, \quad (3)$$

where $A = (a_{ij})$ is the system matrix and has dimensions $I \times J$.

The measurement process is affected by several types of noises: electronic noise from the detector, which is supposed to be Gaussian, and Poisson photonic noise. The lower is the initial X-ray source intensity, the higher is the noise in the acquired projections. In transmission tomography with high photon counts, the noise model is often assumed to be Gaussian for simplicity. For low-dose acquisitions the Poisson nature of the outgoing intensities has to be considered. The noise is thus not only additive and its modelling is a complex task [Yu et al., 2012, Leuschner et al., 2021]. In order to take this into account, our simulations include a Poisson-Gaussian mixture representative of both the low dose acquisition mode and of the electronic noise.

In this work, we consider reconstructions that are solutions of the following optimization problem:

$$f^* = \arg \min_f d(p, Af) + R(f)$$

where $d(p, Af)$ is the data consistency term and $R(f)$ a regularization term. The data consistency term constrains the reconstructed volume to fit the acquired data and allows, through the choice of the distance d , to add knowledge on statistical properties of the noise. The regularization term forces the solution to satisfy a priori information on the unknown object. A commonly used regularization term is the total variation (TV) semi-norm introduced in the next paragraph.

2.2. Total Variation

Total variation regularization in tomographic reconstruction is a reference method when one has to deal with noisy projections and was previously used in particular for low-dose acquisition [Persson et al., 2001, Sidky et al., 2006, Sawatzky et al., 2008, Anthoine et al., 2012, Yan et al., 2011]. For a function $f \in L^1(\Omega)$, with Ω an open subset of \mathbb{R}^3 , the total variation semi-norm is given by :

$$TV(f) = \sup \left\{ - \int_{\Omega} f(x) \operatorname{div} \varphi(x) : \varphi \in C_C^1(\Omega, \mathbb{R}^3), |\varphi(x)| \leq 1 \ \forall x \in \Omega \right\} \quad (4)$$

where $C_C^1(\Omega, \mathbb{R}^3)$ is the space of compactly supported functions with continuous derivatives, and $|y| = \sqrt{y_1^2 + y_2^2 + y_3^2}$ for all $y = (y_1, y_2, y_3) \in \mathbb{R}^3$. This functional is finite if and only if the distributional derivative Df of f is a finite Radon measure on Ω (see for instance [Chambolle, 2004]). Moreover, if $f \in W^{1,1}(\Omega)$, or equivalently $\nabla f \in L^1(\Omega)$, the total variation becomes $TV(f) = \int_{\Omega} |\nabla f(x)| dx$.

Hereafter we will use the discrete version of the total variation. Let f be now a three-dimensional image, that is, an array of size $J = M \times N \times N$. We denote X the Euclidean space $\mathbb{R}^{M \times N \times N} = \mathbb{R}^J$. The discrete gradient of f is the array of elements $(\nabla f)_{i,j,k} = \left((\nabla f)_{i,j,k}^1, (\nabla f)_{i,j,k}^2, (\nabla f)_{i,j,k}^3 \right)$, where

$$(\nabla f)_{i,j,k}^1 = \begin{cases} f_{i+1,j,k} - f_{i,j,k} & \text{if } i < M \\ 0 & \text{if } i = M \end{cases}, \quad (\nabla f)_{i,j,k}^2 = \begin{cases} f_{i,j+1,k} - f_{i,j,k} & \text{if } j < N \\ 0 & \text{if } j = N \end{cases}$$

$$\text{and } (\nabla f)_{i,j,k}^3 = \begin{cases} f_{i,j,k+1} - f_{i,j,k} & \text{if } k < N \\ 0 & \text{if } k = N \end{cases}.$$

We denote $Y = X^3$ the space of gradients of three-dimensional images from X . The discrete total variation is then:

$$TV(f) = \sum_{i,j,k} |(\nabla f)_{i,j,k}| \quad (5)$$

or, equivalently,

$$TV(f) = \sup \{ \langle \varphi, \nabla f \rangle_Y : \varphi \in Y, |\varphi_{i,j,k}| \leq 1, i = 1, \dots, M, j, k = 1, \dots, N \} \quad (6)$$

where $\langle \varphi, \psi \rangle_Y = \sum_{i,j,k} \left(\varphi_{i,j,k}^1 \psi_{i,j,k}^1 + \varphi_{i,j,k}^2 \psi_{i,j,k}^2 + \varphi_{i,j,k}^3 \psi_{i,j,k}^3 \right)$. With the discrete divergence defined as :

$$(\operatorname{div} \varphi)_{i,j,k} = \begin{cases} \varphi_{i,j,k}^1 - \varphi_{i-1,j,k}^1, & \text{if } 1 < i < M \\ \varphi_{i,j,k}^1, & \text{if } i = 1 \\ -\varphi_{i-1,j,k}^1, & \text{if } i = M \end{cases} + \begin{cases} \varphi_{i,j,k}^2 - \varphi_{i,j-1,k}^2, & \text{if } 1 < j < N \\ \varphi_{i,j,k}^2, & \text{if } j = 1 \\ -\varphi_{i,j-1,k}^2, & \text{if } j = N \end{cases} \\ + \begin{cases} \varphi_{i,j,k}^3 - \varphi_{i,j,k-1}^3, & \text{if } 1 < k < N \\ \varphi_{i,j,k}^3, & \text{if } k = 1 \\ -\varphi_{i,j,k-1}^3, & \text{if } k = N \end{cases}$$

we have $\langle \varphi, \nabla f \rangle_Y = -\langle \operatorname{div} \varphi, f \rangle$ which leads to the discrete transcription of (4).

2.3. Reconstruction algorithms

In this work, we then consider solving the TV regularization problem, expressed as

$$f^* = \arg \min_f d(p, Af) + \alpha TV(f) \quad (7)$$

with α a positive parameter which controls the degree of smoothness. We consider that $d(p, Af)$ is either the least squares error norm $\|p - Af\|_2^2$ or the Kullback-Leibler distance

$$KL(p, Af) = \sum_i p_i \ln p_i - p_i \ln (Af)_i + (Af)_i - p_i \quad (8)$$

The last one might be better suited for the high level of noise encountered in low-dose data.

Unlike parallel beam imaging, in CBCT the number of rays traversing a voxel is variable across the volume. More dose is given to the region of interest (ROI) since this is what we are interested in. This is reflected mathematically by the sensitivity, defined as:

$$s = A^* \mathbf{1}, \quad (9)$$

where $\mathbf{1}$ is a column vector of ones and A^* , the adjoint (or transpose) of A , is the matrix of the back-projection operator. The term sensitivity is better known in emission tomography where it represents the probability for a photon to be detected somewhere.

We recall in the next subsections the non-regularized SIRT and MLEM algorithms and present the TV-minimization algorithms considered in this work.

2.3.1. The SIRT algorithm

At each iteration, SIRT computes the weighted difference between the projections of the current volume and the acquired projections, then back-projects the result and subtracts it from the current volume:

$$f^{(n+1)} = f^{(n)} + \lambda \frac{1}{A^* \mathbf{1}} A^* \left[\frac{p - Af^{(n)}}{A \mathbf{1}} \right], \quad (10)$$

with $\lambda > 0$ the SIRT update step. SIRT can be seen as a weighted version of gradient descent for the minimization of the distance $\|Af - p\|_2^2$. The algorithm is slower but more stable than the Algebraic Reconstruction Technique (ART) [Gordon et al., 1970] which uses a single projection at each iteration.

2.3.2. The MLEM algorithm

The Maximum Likelihood Expectation Maximization algorithm (MLEM) and its variants are mainly used in emission tomography where the number of photons is low and they are detected individually. The EM (Expectation-Maximization) algorithm is an iterative technique used to maximize the log-likelihood function, which in tomographic reconstruction represents the probability that an image f generates the measured

projection data p . If we consider that the projections are Poisson distributed, the MLEM algorithm estimates the attenuation image by maximizing the log-likelihood

$$l(f|p) = -\sum_{i=1}^I \sum_{j=1}^J a_{ij} f_j + \sum_{i=1}^I p_i \ln \left(\sum_{j=1}^J a_{ij} f_j \right) - \sum_{i=1}^I \ln(p_i!) \quad (11)$$

under the positivity constrain on the coefficients of f . Maximizing (11) is equivalent to minimizing

$$d(p, Af) = \sum_{i=1}^I \sum_{j=1}^J a_{ij} f_j - \sum_{i=1}^I p_i \ln \left(\sum_{j=1}^J a_{ij} f_j \right) \quad (12)$$

which is the non-constant part of the Kullbak-Leibler distance (8). The EM algorithm applied to this minimization problem leads to the iterative scheme:

$$f_j^{(n+1)} = \frac{f_j^{(n)}}{s_j} \sum_{i=1}^I a_{ij} \frac{p_i}{\sum_{k=1}^J a_{ik} f_k^{(n)}} \quad (13)$$

with $s_j = \sum_{i=1}^I a_{ij}$. Equation (13) can be expressed with matrix multiplication and element-wise operations as:

$$f^{(n+1)} = \frac{f^{(n)}}{A^* \mathbf{1}} A^* \left[\frac{p}{Af^{(n)}} \right] \quad (14)$$

MLEM algorithm is simple, efficient and allows to take into account the stochastic description of the problem. To further accelerate its convergence, Landweber-Kaczmarz acceleration techniques are usually applied and this leads to the ordered-subset expectation maximization or OSEM algorithm. As the number of iterations increases, high frequencies from the projections are progressively included and the image becomes less blurred and more precise. However, the algorithm has to be stopped before too many parasite high frequencies from noise are introduced. Finding a suitable number of iterations is usually a difficult task considering the balance between noise and precision. Stopping the iterations based on the discrepancy principle is a regularization method. In practice, the MLEM images are usually post-processed to remove the noise.

2.3.3. The SIRT-TV algorithm

One approach to solve (7) with quadratic data fidelity is to perform TV denoising of the volume between successive SIRT steps. If $f^{(n+1/2)}$ is the volume after a SIRT iteration, the TV regularization aims at minimizing:

$$\min_f \left\{ \frac{1}{2} \|f - f^{(n+1/2)}\|_2^2 + \alpha TV(f) \right\}. \quad (15)$$

This minimization can be done by the Chambolle's algorithm [Chambolle, 2004] as

$$f^{(n+1)} = f^{(n+1/2)} - \alpha \operatorname{div} \varphi^*, \quad (16)$$

with φ^* iteratively computed as the limit of :

$$\varphi^{(k+1)} = \frac{\varphi^{(k)} + \tau \nabla(\operatorname{div} \varphi^{(k)} - f^{(n+1/2)}/\alpha)}{1 + \tau |\nabla(\operatorname{div} \varphi^{(k)} - f^{(n+1/2)}/\alpha)|}, \quad (17)$$

starting from $\varphi^{(0)} = 0$ and τ being an update parameter such that $0 < \tau < 1/12$ for three-dimensional images.

An acceleration method, the Fast Iterative Shrinkage-Thresholding Algorithm (FISTA) [Beck and Teboulle, 2009b] was shown to speed up the convergence [Banjak, 2016]. This technique consists in replacing the current volume $f^{(n+1)}$ by a linear combination of $f^{(n+1)}$ and the previous value $f^{(n)}$ defined as:

$$\bar{f}^{(n+1)} = f^{(n+1)} + \frac{t^{(n)} - 1}{t^{(n+1)}} (f^{(n+1)} - f^{(n)}). \quad (18)$$

The relaxation parameter $t^{(n)}$ is iteratively computed with $t^{(0)} = 1$ and $t^{(n+1)} = \frac{1}{2} \left(1 + \sqrt{1 + 4(t^{(n)})^2} \right)$. The new volume $\bar{f}^{(n+1)}$ replaces $f^{(n)}$ in the next iteration, as input of the SIRT formula (10).

2.3.4. The KL-TV algorithm

The algorithm proposed by Chambolle and Pock in [Chambolle and Pock, 2011] aims at solving general optimization problems that can be written under the form

$$\min_f \{F(Kf) + G(f)\} \quad (19)$$

where K is a linear operator, F and G are convex and possibly non-smooth. Sidky et al. adapted this algorithm to tomographic reconstruction in [Sidky et al., 2012]. The optimization problem (7) with Kullback-Leibler data consistency term can be expressed in the form of (19) with $F(Kf) = F_1(y) + F_2(z)$ and $G(f) = 0$, where:

$$\begin{aligned} K &= \begin{pmatrix} A \\ \nabla \end{pmatrix}, \\ y &= Af, \quad z = \nabla f, \\ F_1(y) &= \sum_i [y - p + p \ln p - p \ln(\text{pos}(y))]_i + \delta_P(y), \\ F_2(z) &= \alpha \|(|z|)\|_1. \end{aligned} \quad (20)$$

In the equation above, $[\text{pos}(x)]_i = \max(0, x_i)$ and

$$\delta_P(y) = \begin{cases} 0 & \text{if } y \text{ is positive} \\ +\infty & \text{otherwise} \end{cases}. \quad (21)$$

Compared to the cost function in (7), a positivity constraint on the projections has been added in order to enforce the positivity of the solution. In this paper, we use the pre-conditioned version from [Pock and Chambolle, 2011, Sidky et al., 2012], which allows significant acceleration of the convergence. The pseudo-code of the resulting KL-TV algorithm is given hereafter as algorithm 1. We denote by $\mathbf{1}$ a vector of ones with dimensions defined by the subscript. The subscript I , P and V denote respectively the image, the projections and the image gradient. $|M|$ is the matrix formed by taking the absolute value of each element of M . Except for matrix-vector multiplications, all other operations are done element-wise.

Compared to the original Chambolle-Pock algorithm, the preconditioned version has no parameters to tune once the relaxation parameter is fixed. All the other parameters have been replaced by the matrices Σ_1 , Σ_2 and T .

Algorithm 1: PRE-CONDITIONED KL-TV

Input: The acquired projections p , the TV parameter α

Output: The reconstructed and denoised volume by KL-TV algorithm

```

1  $\Sigma_1 \leftarrow \mathbf{1}_P / (A\mathbf{1}_I)$ ;  $\Sigma_2 \leftarrow \mathbf{1}_V / (|\alpha\nabla|\mathbf{1}_I)$ ;  $T \leftarrow \mathbf{1}_I / (A^*\mathbf{1}_P + |\alpha\text{div}|\mathbf{1}_V)$ 
2 Initialize  $u^{(0)}$ ,  $z^{(0)}$  and  $q^{(0)}$  to zero values
3  $\bar{u}^{(0)} \leftarrow u^{(0)}$ 
4 while  $n \leq N$  do
5    $y^{(n+1)} \leftarrow \frac{1}{2} \left( \mathbf{1}_P + y^{(n)} + \Sigma_1 A \bar{f}^{(n)} - \sqrt{(y^{(n)} + \Sigma_1 A \bar{f}^{(n)} - \mathbf{1}_P)^2 + 4\Sigma_1 p} \right)$ 
6    $z^{(n+1)} \leftarrow (z^{(n)} + \alpha\Sigma_2 \nabla \bar{f}^{(n)}) / \max(\alpha\mathbf{1}_I, |z^{(n)} + \alpha\Sigma_2 \nabla \bar{f}^{(n)}|)$ 
7    $f^{(n+1)} \leftarrow f^{(n)} - T A^* y^{(n+1)} + T \text{div} z^{(n+1)}$ 
8    $\bar{f}^{(n+1)} \leftarrow 2f^{(n+1)} - f^{(n)}$ 
9    $\bar{f}^{(n+1)} \leftarrow \text{pos}(\bar{f}^{(n+1)})$ 
10   $n \leftarrow n + 1$ 
11 return  $\bar{f}^{(n+1)}$ 

```

2.3.5. The MLEM-TV algorithm

The solution of the TV regularized reconstruction problem (7) with Kullback-Leibler data fidelity term can be obtained numerically with the EM algorithm [Dempster et al., 1977]. At each iteration, two operations are completed: an (E) step which is the regular MLEM iteration,

$$f^{(n+1/2)} = \frac{f^{(n)}}{A^*\mathbf{1}} A^* \left[\frac{p}{A f^{(n)}} \right] \quad (22)$$

and a (M) step consisting into a TV denoising of the volume:

$$f^{(n+1)} \in \arg \min_{f \in \mathbb{R}_+^J} \left\{ \langle f, s \rangle - \langle \ln(f), s f^{(n+1/2)} \rangle + \alpha TV(f) \right\}. \quad (23)$$

The proof of the convergence and an efficient dual algorithm for the resolution of (23) are given in [Maxim et al., 2018]. By using the Fenchel-Rockafellar duality theorem, problem (23) can be reformulated through its dual and we get:

$$f^{(n+1)} = \frac{s f^{(n+1/2)}}{s + \alpha \text{div} \varphi^*}, \quad (24)$$

with φ^* iteratively computed starting from $\varphi^{(0)} = 0$ and for $k \in \mathbb{N}$,

$$\varphi^{(k+1)} = \frac{\varphi^{(k)} - \tau z^{(k)}}{1 + \tau |z^{(k)}|}, \quad z^{(k)} = \nabla \left(\frac{s f^{(n+1/2)}}{s + \alpha \text{div} \varphi^{(k)}} \right). \quad (25)$$

Here $\tau > 0$ is a minimization step. Let us note $s_{\min} = \min_j s_j$. To ensure the convergence of the algorithm, two constraints have to be verified:

- $\alpha < s_{min}/6$
- $\tau < \alpha/L_h$ with $L_h = 12\alpha^2 \frac{\|sf^{(n+1/2)}\|_\infty}{(s_{min} - 6\alpha)^2}$,

where $\|sf^{(n+1/2)}\|_\infty$ is the infinity norm of $sf^{(n+1/2)}$ seen as a one-dimensional vector.

One particularity of CBCT is that the sensitivity is far from being constant across the volume and one order of magnitude of difference can be observed between the values in the FOV and the values in the corners of the volume. The discrepancy becomes even more important when extensions of the volume are considered because of the truncated projections. As the minimization step τ depends on s_{min} , the convergence significantly slows down in the entire volume, even if the small values of the sensitivity are located in regions that are cropped after reconstruction. Following the idea of the preconditioned Chambolle-Pock algorithm, we test a new version of algorithm (25) where we replace τ with the matrix:

$$T = 0.9 \times \frac{(s - 6\alpha)^2}{12\alpha sf^{(n+1/2)}}. \quad (26)$$

This formulation allows faster convergence in the central part of the volume and thus for the region of interest. As for SIRT-TV, a FISTA acceleration step (18) is added to speed up the reconstruction. A FISTA acceleration is also used during the computation of the sequence $(\varphi^{(k)})_{k \in \mathbb{N}}$ from (25) to accelerate the convergence of the TV denoising.

3. Experimental data acquisition and phantom simulation

3.1. 3D CBCT acquisition geometry

The CBCT dental acquisition geometry is illustrated in figure 1. The source and the detector rotate around the patient's head on a circular trajectory. The axis of rotation is located at 401.07 mm from the source and the distance source-detector is 564.30 mm. The size of the detector is 12×14 cm, with 600×700 pixels of size 200 μm . The projections are acquired with short scan conditions.

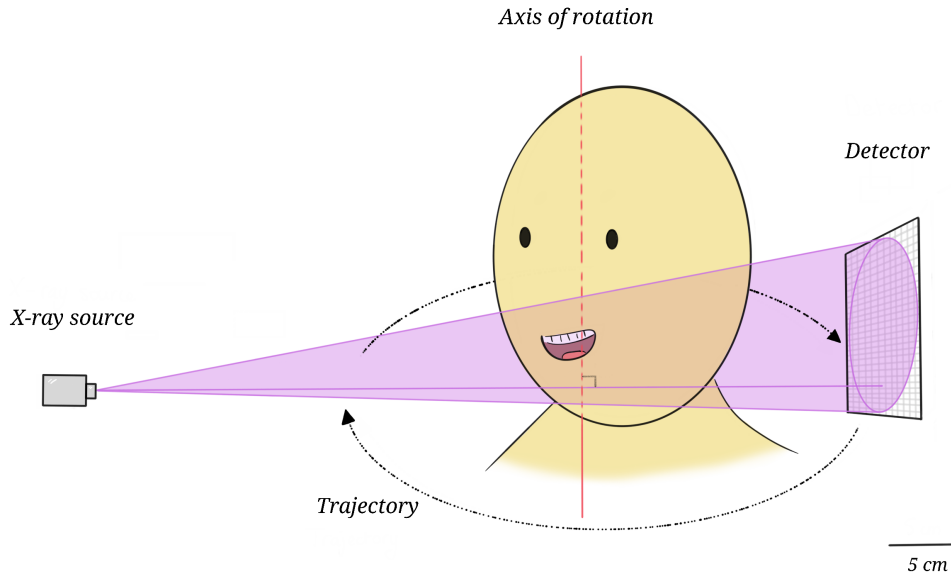


Figure 1. Diagram of the acquisition geometry.

3.2. CBCT acquisition from a dental phantom

A CBCT acquisition of an anthropomorphic head phantom delivered by W. Loy GmbH† was realized with a Carestream Dental Scanner CS 8200 3D. A set of 155 projections was taken under a low-dose protocol, with 80 kV and 2 mA over 3.1s. To reduce the memory footprint during reconstruction, the projections were subsampled to 300×350 pixels. The reconstructed volume is composed of $350 \times 275 \times 275$ cubic voxels with a size equal to $300 \mu\text{m}$, giving a volume measuring $105 \times 82.5 \times 82.5 \text{ mm}^3$.

Rather than adding a simulated noise on the real data, we have chosen to simulate an ultra-low dose acquisition by lowering the number of projections, which corresponds effectively to a dose reduction on scanners having pulsing capabilities. Both techniques are used in medical imaging to effectively reduce the dose received by the patient [Liu et al., 2015, Humphries et al., 2019]. Thus, we consider an ultra low-dose version of these data, where 78 projections are regularly sampled from the low-dose data.

In order to mitigate the effect of truncation and following the idea from [Maltz et al., 2007], for the FDK reconstruction we extended the projections considering the FOV embedded into a cylinder. As in our experience this technique gave poor results with iterative reconstructions, we simply augmented the size of the reconstructed volume as in [Dang et al., 2016], by adding 150 voxels on each side. After reconstruction we truncated the volume to obtain only the ROI.

3.3. Three-dimensional jaw phantom

The application of the algorithms to a numerical phantom allowed us to test their reliability and to adjust the different parameters. We simulated a 3D jaw phantom

† <https://www.loy-gmbh.de/produkt/dental-phantom/>

inspired from the FORBILD phantom[†], containing in a cylinder representing the head of the patient some geometrical forms reproducing the spine, the jaw, as well as 31 teeth. Three teeth from the lower jaw have the density of the metal. The simulated volume has dimensions $105 \times 82.5 \times 82.5 \text{ mm}^3$ sampled in $350 \times 275 \times 275$ voxels. A total of 78 projections with the same angles as for the experimental data (in ultra low-dose case) were calculated using the ASTRA Toolbox [Van Aarle et al., 2016] in Python. In order to best represent the problem raised by the dental data at our disposal, the phantom projections were simulated with the same geometry as previously described, and the amount of noise to be added was determined from the experimental projections. To simulate the photonic noise, Poisson noise was added after scaling the projections by a multiplicative factor aiming to reach the same order of magnitude as in the experimental data. Finally, a Gaussian noise was added to simulate the electronic noise. The Gaussian noise level was estimated using the statistical relationship between the noise variance and the eigenvalues of the covariance matrix of patches extracted from the images [Chen et al., 2015]. Negative values were replaced by zeroes.

3.4. Algorithms implementation and evaluation metrics

The algorithms have been implemented in Python and the ASTRA toolbox library has been used to compute the projection and backprojection operations. The reconstructions have been done on a Intel Xeon Gold 6226R processor and a Tesla V100 GPU.

As for the Shepp-Logan phantom the reference volume f_{ref} is available, we evaluate the methods with the following metrics:

- Normalized Root Mean Squared Error (NRMSE) is defined as follows:

$$NRMSE(f, f_{ref}) = \frac{\|f - f_{ref}\|_2}{\|f_{ref}\|_2}$$

The NRMSE computes the cumulative squared error between the reconstructed volume and the ground truth. A smaller NRMSE values points out that the reconstructed image is closer to the ground truth.

- The Peak Signal to Noise Ratio (PSNR) mirrors the difference in the noise level, in dB, between the two images.

$$PSNR(f, f_{ref}) = 10 \log_{10} \left(\frac{\Delta^2}{\frac{1}{J} \sum_{j=1}^J (f_j - f_{ref,j})^2} \right),$$

with Δ the data range of the true image, and J the total number of voxels. A larger PSNR values indicates a better quality of the reconstruction.

- The Structural SIMilarity (SSIM) is used to measure the similarity between two images, using the luminance, the contrast and the structure of the two images:

$$SSIM(f, f_{ref}) = \frac{(2\mu_f \mu_{f_{ref}} + c_1)(2\sigma_{ff_{ref}} + c_2)}{(\mu_f^2 + \mu_{f_{ref}}^2 + c_1)(\sigma_f^2 + \sigma_{f_{ref}}^2 + c_2)},$$

[†] <http://www.imp.uni-erlangen.de/phantoms/>

with $c_1 = 0.01 \times \Delta$ and $c_2 = 0.03 \times \Delta$, Δ still being the data range of the true image.

We compare the convergence speed of the different algorithms in terms of both reconstruction iterations and time, by observing the decrease of the cost function.

For the experimental data, we took as reference a normal dose FDK reconstruction of the phantom. However, the range of values of this reconstruction being different from ours, we could not use the same metrics as for the numerical phantom. We therefore used the Contrast-to-Noise Ratio (CNR) and the correlation with the reference image. For the calculation of the CNR, we compared the mean values on a patch inside a tooth (μ_{obj}) and on a patch from the background (μ_{BG}), with respect to the standard-deviation (σ_{BG}) of the noise in the background:

$$CNR(obj, BG) = 20 \log_{10} \left(\frac{|\mu_{obj} - \mu_{BG}|}{\sigma_{BG}} \right).$$

To evaluate the correlation, we calculated the Pearson product-moment correlation coefficients between the images f and g having the same size as:

$$\text{Corr}(f, f_{ref}) = \frac{\text{cov}(f, f_{ref})}{\sigma_f \sigma_{f_{ref}}},$$

and with μ_f and μ_g being respectively the mean of f and g ,

$$\text{cov}(f, f_{ref}) = \frac{1}{J-1} \sum_{j=1}^J [(f_j - \mu_f)(f_{ref,j} - \mu_{f_{ref}})].$$

4. Results

In this section, we analyze the performance of the different methods on the numerical jaw phantom in 3D and then we investigate issues specific to experimental data.

4.1. 3D jaw phantom

The iterative methods require to set some parameters: the number of iterations (N), the number of iterations of the TV denoising step (NTV) and the regularization parameter α . For SIRT-TV we also had to choose the value of λ that we set to 0.8. For larger values the algorithm was divergent. All the parameters were chosen manually in the first place, by varying their values until we obtained a subjective good compromise between removing noise and conserving image features. In a second step, we tried to lower the number of iterations and the TV parameters, while keeping a reasonable image quality and a MSE value comparable to the one obtained with many iterations. Table 1 summarizes the final parameter values for the different algorithms.

Method	SIRT-TV	MLEM	MLEM-TV	KL-TV
N	400	200	400	500
NTV	20		20	
α	5×10^{-5}		0.1	0.1

Table 1. Parameters used for the reconstruction of the 3D jaw phantom. N is the number of reconstruction iterations, NTV is the number of TV iteration if applicable and α is TV parameter used to tweak the importance of the regularization.

Figure 2 shows the evolution of the cost functions as a function of the number of iterations and time for the different algorithms. We can notice the SIRT-TV is the slowest method to converge.

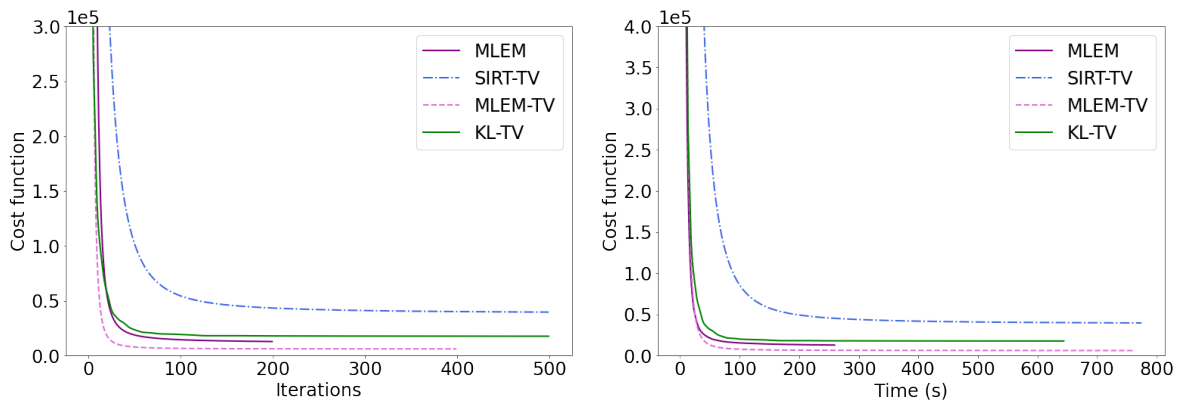


Figure 2. Cost function evolution for the reconstruction of the phantom in low-dose mode. At the left, the cost function according to the iterations, and at the right, the cost function according to the time in seconds.

The NRMSE, PSNR and SSIM values of the different reconstructions are shown in table 2. All these metrics reflect the lower quality of the images provided by FDK for a small number of projections. MLEM is less affected by streak artifacts, which explains the much better values for the quality metrics compared to FDK reconstruction. The metrics for the three other methods are better. Regularized statistical methods obtain better results than SIRT-TV, suggesting that these algorithms are more suitable for the mixed Poisson-Gaussian noise model present in this study. They are roughly similar, with a slightly better performance for KL-TV.

Metrics	FDK	MLEM	SIRT-TV	MLEM-TV	KL-TV
NRMSE	0.248	0.229	0.046	0.031	0.030
PSNR	39.684	41.354	50.504	54.328	57.216
SSIM	0.841	0.976	0.996	0.998	0.999

Table 2. NRMSE, PSNR and SSIM for the reconstruction of the jaw phantom with the different algorithms.

A profile extracted from each volume and containing two teeth is shown in figure 3. We can note the noise in the FDK and MLEM methods and the positive impact of the regularization.

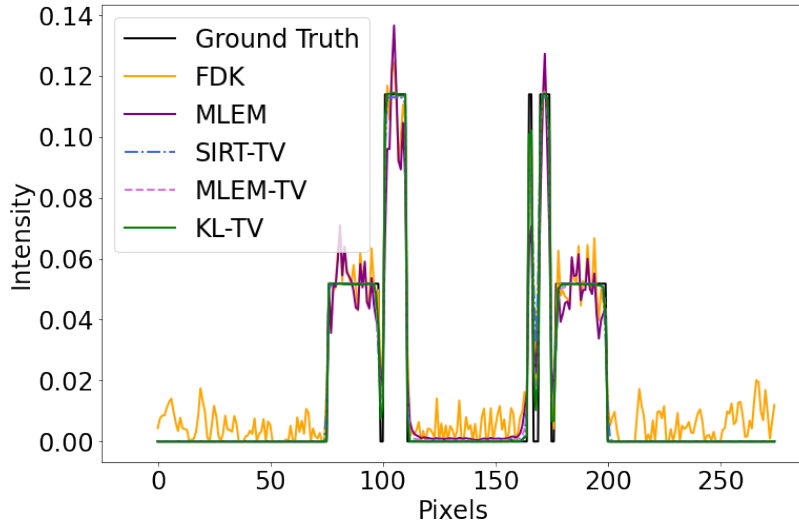
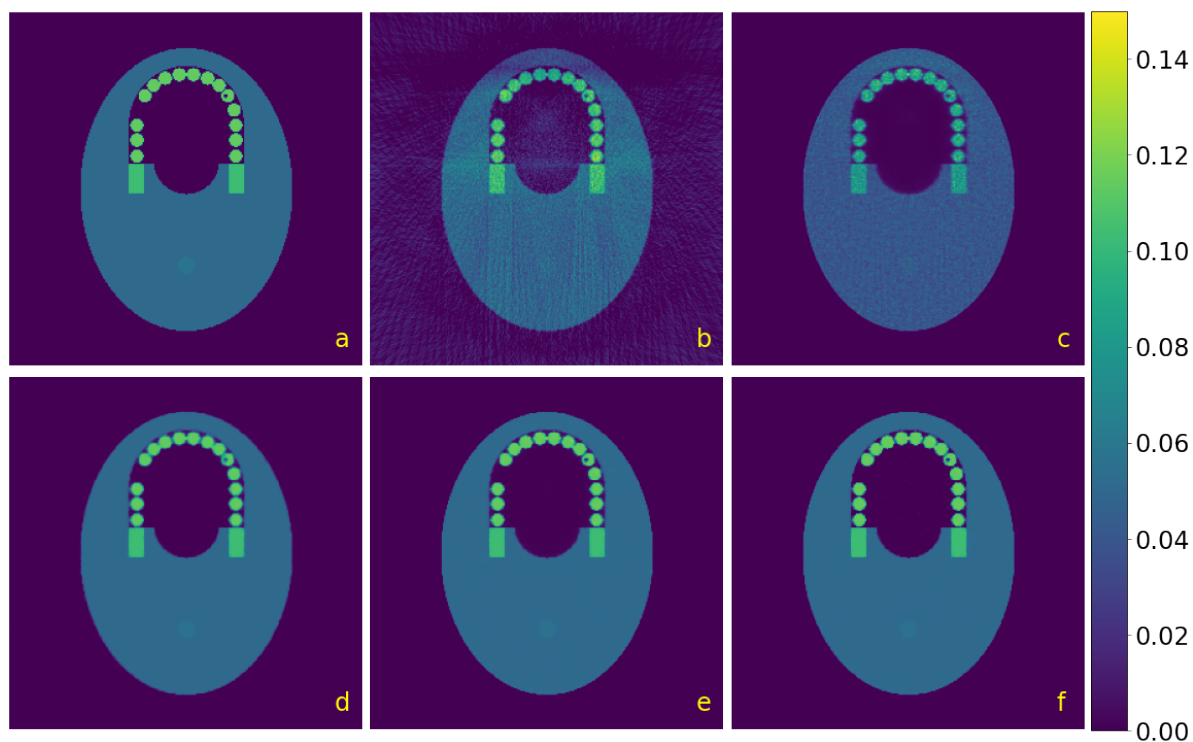


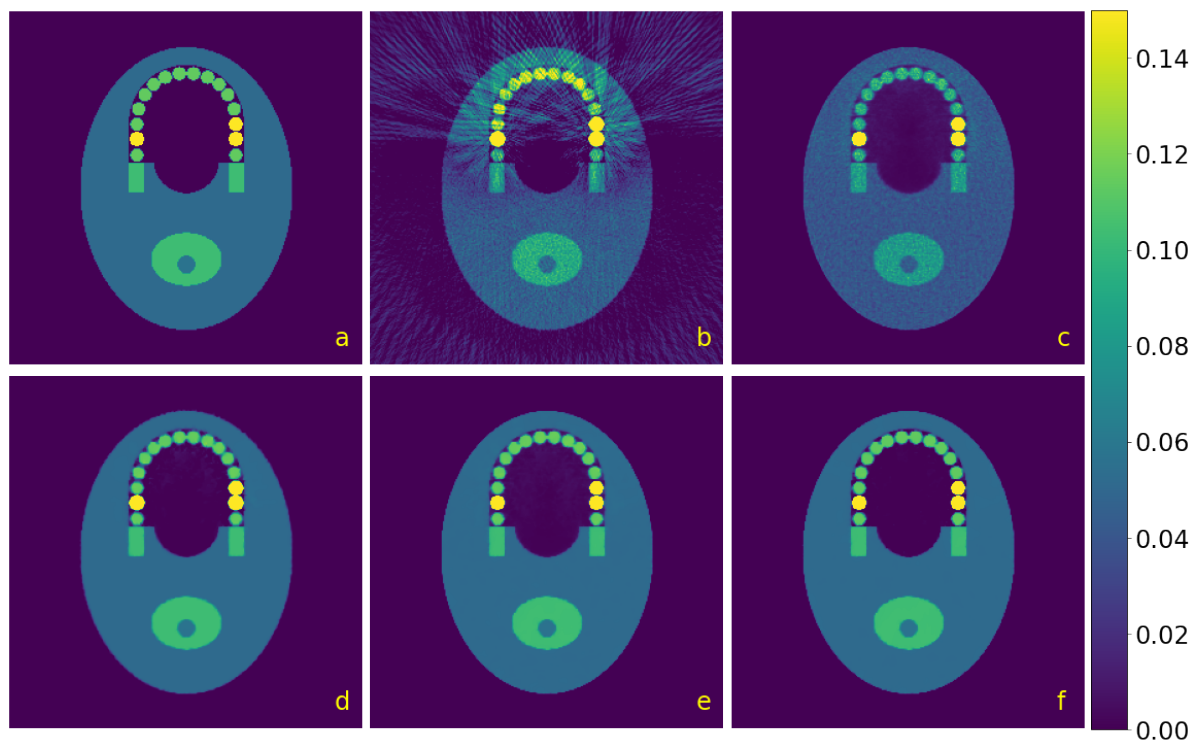
Figure 3. Profile extracted from the reconstructed volumes.

Figure 4 shows axial slices of the reconstructed volumes. From the axial slice shown in figure 4(i) it can be seen that all the methods succeeded to recover even the cavity inside the premolar from the jaw phantom, although the FDK and MLEM reconstructions are slightly noisy. Strike artifacts due to the limited number of projections can be observed in the FDK image. These artifacts are more visible in the second axial slice shown in 4(ii) due to the presence of metal in this part of the jaw. We do not observe such artifacts in the iterative reconstructions. In particular, we can highlight the ability of MLEM to remove metal artifact, even without the use of regularization. A coronal slice can be seen in figure 5. The cone beam artifact visible at the top of the volume is particularly present in the reconstruction with FDK. The MLEM algorithm reduces it outside the object but the upper boundary of the phantom it is quite blurred. Details from this slice are shown in figure 5(ii) where it can be noticed that the vertical lines are quite well reconstructed by the three iterative methods, while the horizontal lines are sharper with KL-TV. The zoom allows to better appreciate the effect of the TV regularization. All three methods achieve an accurate denoised reconstruction, even if SIRT-TV has less sharp edges than MLEM-TV and KL-TV.

In table 3, the reconstruction times are shown. The MLEM algorithm is obviously faster than the other iterative algorithms since it does not do any regularization and the number of iterations is smaller. The regularized methods show comparable computation times with a slight disadvantage for MLEM-TV. The KL-TV method was faster to converge than MLEM-TV and SIRT-TV despite the larger number of iterations

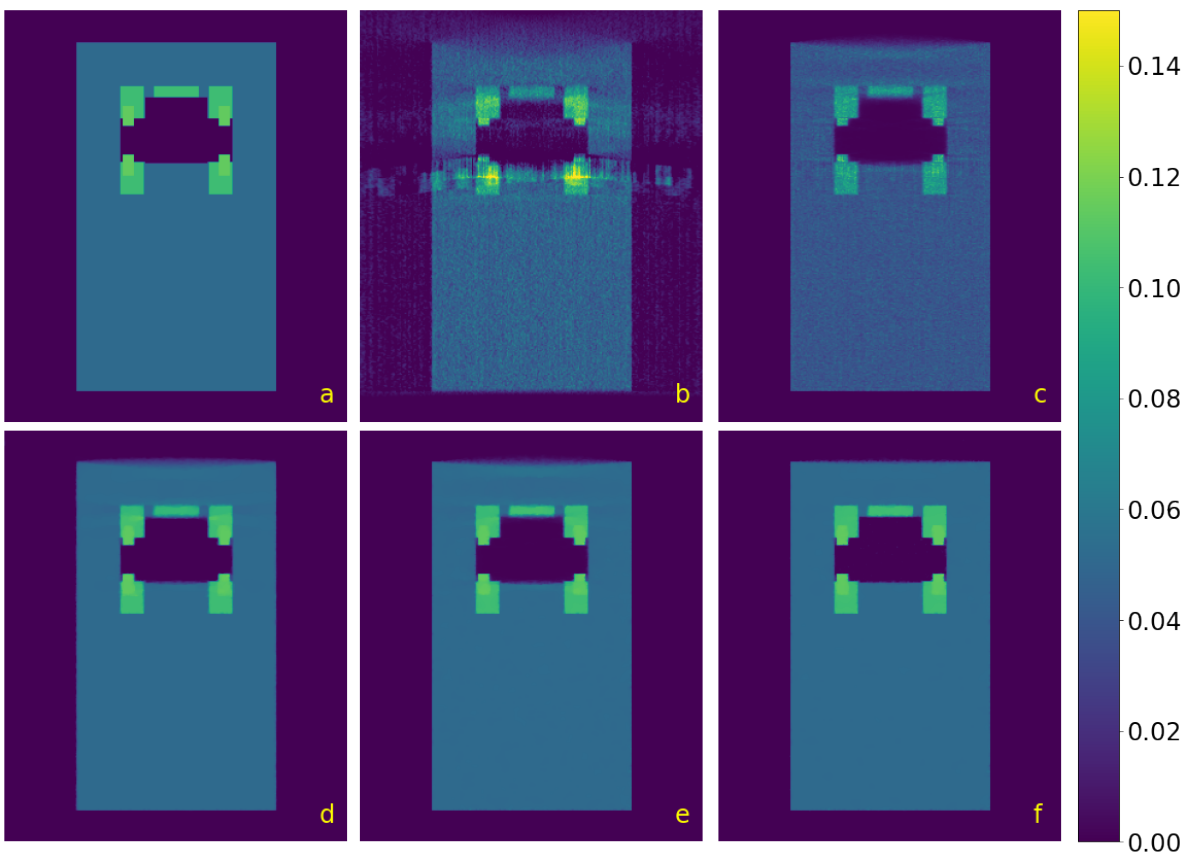


(i) Upper jaw

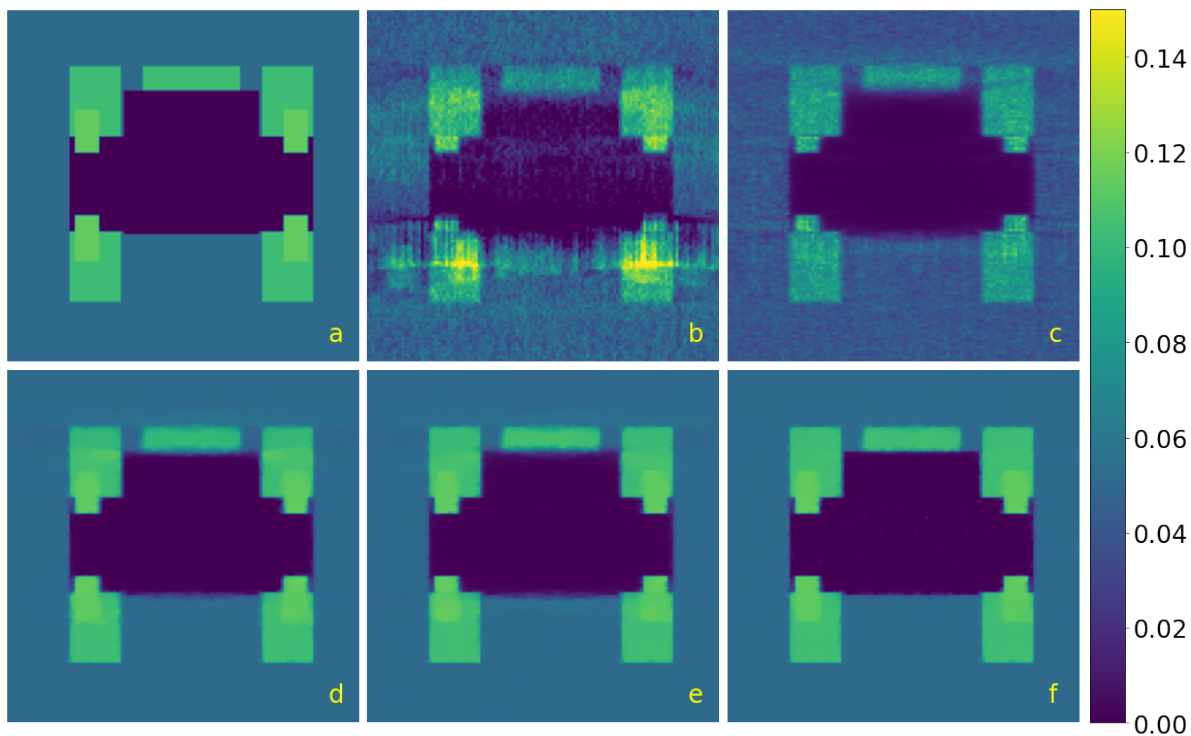


(ii) Lower jaw

Figure 4. Axial slices from jaw phantom. (a) Ground truth, (b) FDK, (c) MLEM, (d) SIRT-TV, (e) MLEM-TV and (f) KL-TV.



(i) Coronal slice from the phantom reconstruction.



(ii) Zoom on the previous coronal slice.

Figure 5. Coronal slice and zoom from jaw phantom. (a) Ground truth, (b) FDK, (c) MLEM, (d) SIRT-TV, (e) MLEM-TV and (f) KL-TV.

compared to the first one and equal for the second. This comes from the inner loop used to perform the denoising in the SIRT-TV and MLEM-TV algorithm.

FDK	MLEM (200)	SIRT-TV (400-20)	MLEM-TV (400-20)	KL-TV (500)
00:00:02	00:04:19	00:12:55	00:12:40	00:10:47

Table 3. Reconstruction time of the Shepp-Logan phantom for the different algorithms. The number of iterations used for the reconstruction and the TV denoising are reminded in the second line.

This section studied the application of the chosen algorithms on the jaw phantom. This simple case allowed us to validate the algorithm on this geometry and helped us to choose the parameters for the next section.

4.2. Experimental dental data

We now apply the algorithms on experimental dental data: in a low-dose configuration which is currently used in dental imaging, and in an ultra low-dose configuration where only one out of two projections were used.

Table 4 summarizes the parameters of the algorithms, in the low-dose and ultra low-dose case. We set the SIRT parameter to $\lambda = 0.9$, compared to the phantom reconstruction, the details are more precise in the experimental data and we needed a higher parameter to speed up the convergence. As in the phantom case, we tried several reconstructions with different number of iterations and TV parameters, and kept the best in term of visualization and metrics. The same number of iterations was kept for the two cases. The TV parameter of SIRT was increased in the ultra low-dose reconstruction. The increase of this parameter in the MLEM-TV and KL-TV reconstructions resulted in too many details being lost. Similarly, increasing the number of iterations did not bring any improvement.

	Method	SIRT-TV	MLEM	MLEM-TV	KL-TV
Low-dose	N	400	400	400	700
	NTV	20		20	
	α	1×10^{-6}		0.05	0.05
Ultra low-dose	N	400	400	400	700
	NTV	20		20	
	α	2×10^{-6}		0.05	0.05

Table 4. Parameters used for the reconstruction of the experimental data.

Compared to the phantom, more iterations had to be performed for most algorithms and especially for KL-TV. The number of iterations for the internal denoising loop was kept the same as its augmentation did not improve the results. Values of the TV

parameter α are different from the jaw phantom reconstruction but remain in the same order of magnitude.

The values of the metrics used to evaluate the reconstructions are presented in table 5. Methods including TV regularization obtain the best results. The MLEM-TV reconstruction gets the best CNR, followed by the KL-TV one. We can notice that the CNR of ultra low-dose reconstructions is higher than that of low-dose. The CNR is a measure of contrast in an image. Since ultra low-dose reconstructions are noisier, the regularization parameter must be higher. However, as the TV denoised images tend to be piece-wise constant, an increase in the TV parameter also improves the contrast at the expense of reconstruction details. The TV parameter was indeed increased for SIRT-TV. For MLEM-TV and KL-TV algorithms, this was not necessary: as the projections are two times less numerous, the value of $KL(Af, p)$ in the cost function is lower, so with the same TV parameter as in low-dose, more importance is given to the regularization. The correlation has been calculated on three different regions: A is the entire volume, B is the 2D region shown in figure 8 and C is the background of the axial slice visible in figure 6. SIRT-TV performs better than the others on the entire volume (Corr A), with a tie with MLEM-TV in ultra low-dose. This result seems in contradiction with the visual observation of the reconstructions. This might be due to the large amount of pixels in the background compared to that in the teeth region, thus the background has a large influence in the correlation. When used to evaluate reconstruction of a tooth (Corr B), a better agreement with visual observation was obtained, as MLEM-TV and KL-TV reached a higher correlation with the ground truth; whereas when applied on a background area (Corr C), SIRT-TV has the greatest correlation, with a more significant gap compared to the total volume. To sum up, MLEM-TV and KL-TV gave the best results for the structures of interest, with a slight advantage to MLEM-TV.

	Metrics	FDK	MLEM	SIRT-TV	MLEM-TV	KL-TV
Low-dose	CNR	16.664	24.879	26.733	28.163	27.290
	Corr A	0.933	0.963	0.974	0.971	0.960
	Corr B	0.897	0.937	0.948	0.954	0.949
	Corr C	0.950	0.952	0.969	0.962	0.951
Ultra low-dose	CNR	13.999	25.798	27.275	30.182	29.308
	Corr A	0.921	0.960	0.968	0.968	0.953
	Corr B	0.817	0.932	0.929	0.952	0.950
	Corr C	0.921	0.946	0.968	0.957	0.943

Table 5. CNR and correlation of experimental data, in low-dose and ultra low-dose cases. Corr A is the value of the correlation on the entire volume, while Corr B is calculated on a 2D region containing a tooth and Corr C on a background region.

For the low-dose data, two axial slices are represented in figures 6 and 7. Total variation regularization strongly reduces the noise. The background is not as smooth as the normal dose image, but increasing the TV parameter would cause the loss of

details that are necessary for a good diagnosis. MLEM-TV and KL-TV images are very similar, with the edge of the teeth sharp, unlike SIRT-TV which appears rather blurred.

The slice shown in figure 7 contains metal inserts that are known to produce metal artifact in FDK reconstructions. No metal artifact reduction method has been used on any reconstruction. Compared to the previous slice, presence of metal decreases the contrast of the reconstructions, especially in SIRT-TV. We can notice that MLEM, even without regularization, succeeds in reducing the metal artifacts contrary to FDK. In particular, the left molars pointed by a red arrow in figure 7 are more visible. However, the incisors are less sharp on MLEM.

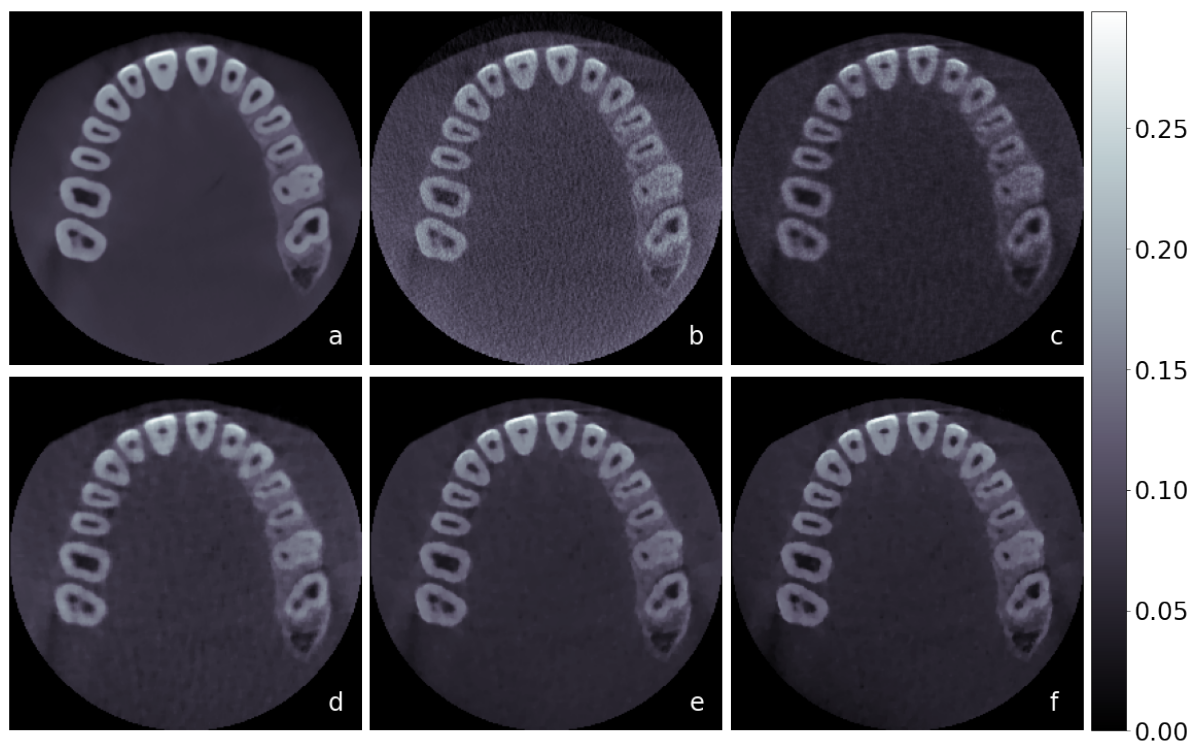


Figure 6. Axial slice from the dental reconstruction, in low-dose. (a) Ground truth, (b) FDK, (c) MLEM, (d) SIRT-TV, (e) MLEM-TV, (f) KL-TV.

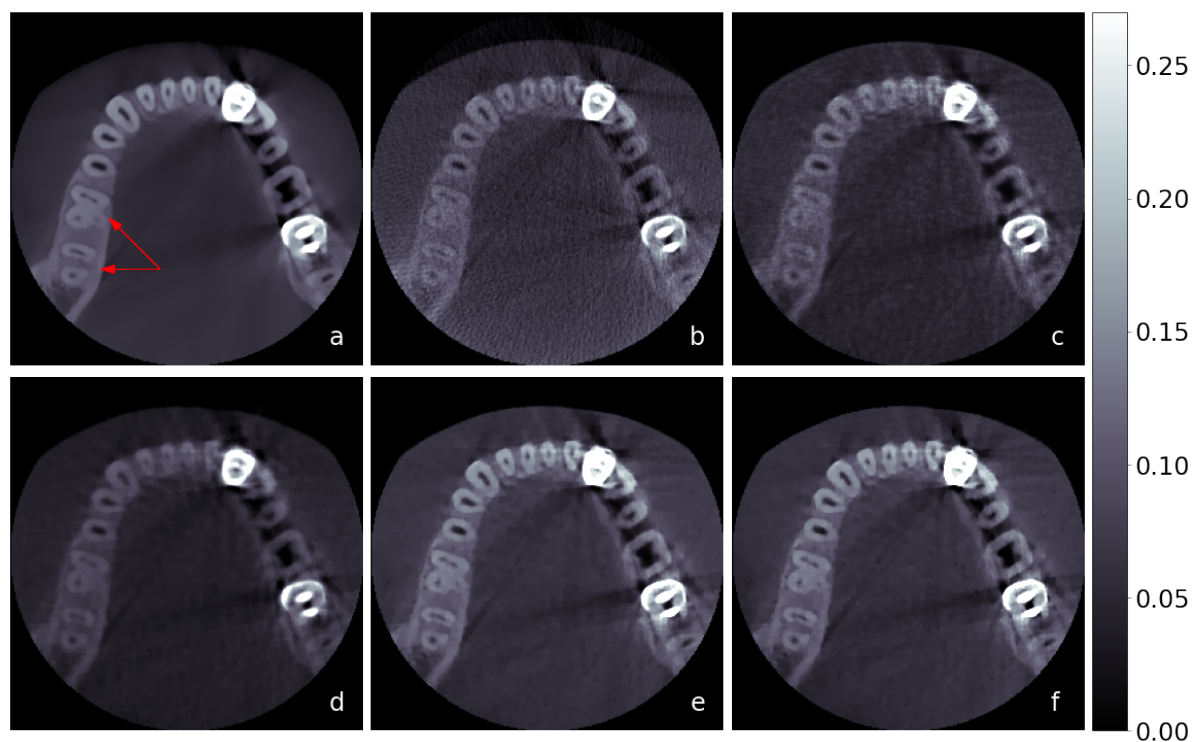


Figure 7. Axial slice containing metal from the dental reconstruction, in low-dose. (a) Ground truth, (b) FDK, (c) MLEM, (d) SIRT-TV, (e) MLEM-TV, (f) KL-TV. The red arrows point to the left molars.

Figure 8 is a zoom on the mandibular left first molar in a coronal slice. Enamel and dentin can be clearly distinguished on all reconstructions. The tooth canals and the bone trabeculae identified respectively by blue and green arrows in figure 8 are more accurately recovered in MLEM-TV and KL-TV images. The mandibular canal (light-blue arrow) is clearly visible on all iterative reconstructions, including MLEM which does not perform denoising.

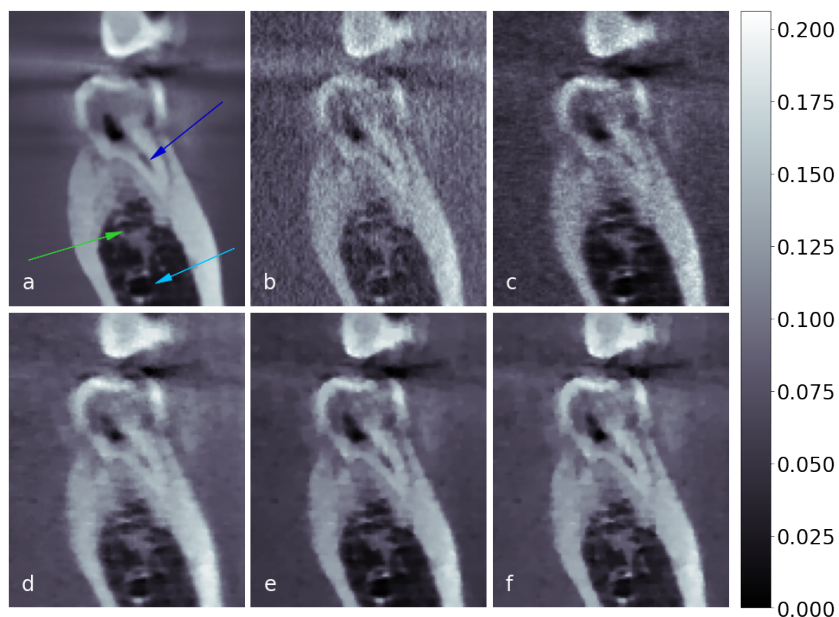


Figure 8. Zoom on a tooth in a coronal slice, low dose acquisition. (a) Ground truth, (b) FDK, (c) MLEM, (d) SIRT-TV, (e) MLEM-TV, (f) KL-TV. The blue, green, light-blue arrows, respectively point to tooth canal, trabeculae bone and mandibular canal.

Figures from 9 to 11 are the reconstructions in ultra low-dose. Overall, the quality of the reconstruction is deteriorated compared to low-dose. In figure 9, the noise present in FDK and MLEM reconstructions and the blur of SIRT-TV mask the root canals of the right first molar (yellow arrows). They are made visible by the regularized statistical methods.

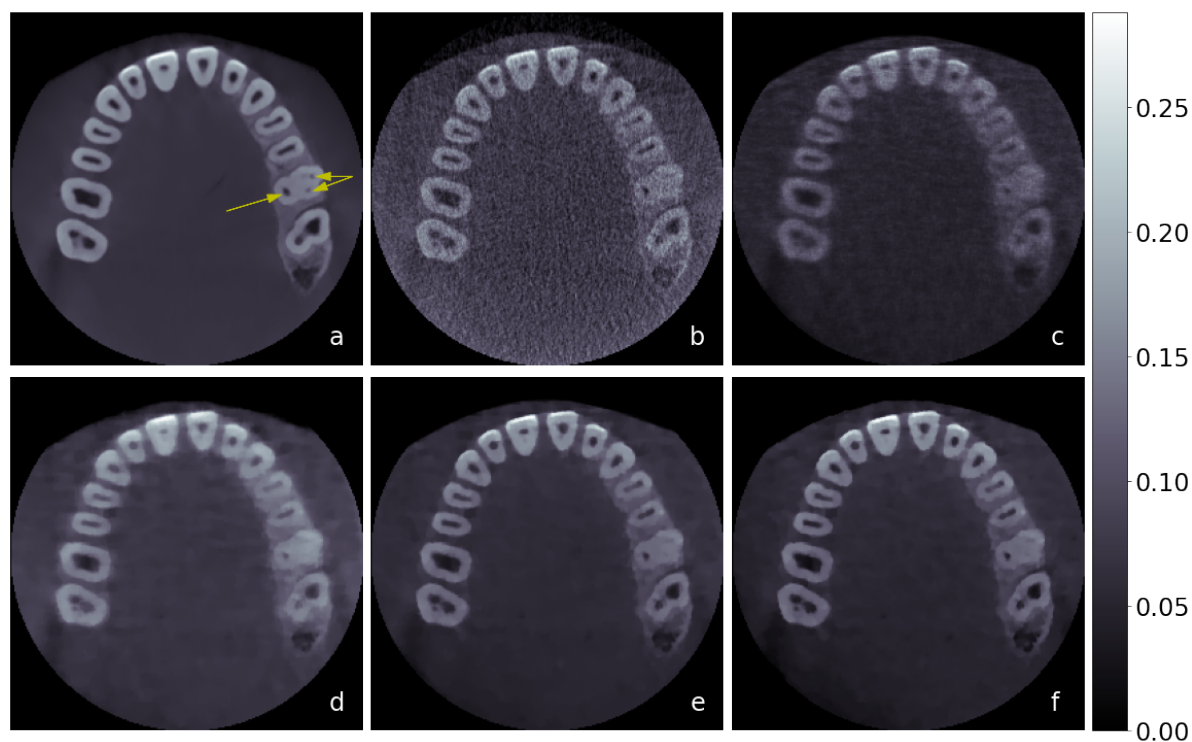


Figure 9. Axial slices of the dental reconstructions, in ultra low-dose. (a) Ground truth, (b) FDK, (c) MLEM, (d) SIRT-TV, (e) MLEM-TV, (f) KL-TV. Root canals of the right first molars are identified by the yellow arrows.

The metal artifacts are stronger in the FDK reconstruction compared to the low dose. Comparison with iterative methods based on visual inspection of figure 10 confirms that iterative methods naturally attenuate these artifacts without any specific correction. The left molars are almost not visible in the FDK reconstruction and are barely distinguishable in MLEM and SIRT-TV images. The root canals pointed by orange arrows were recovered only by MLEM-TV and KL-TV. Some details are also lost in the MLEM-TV and KL-TV reconstruction compared to the low-dose, as the canal at the right of the first left molar (white arrow).

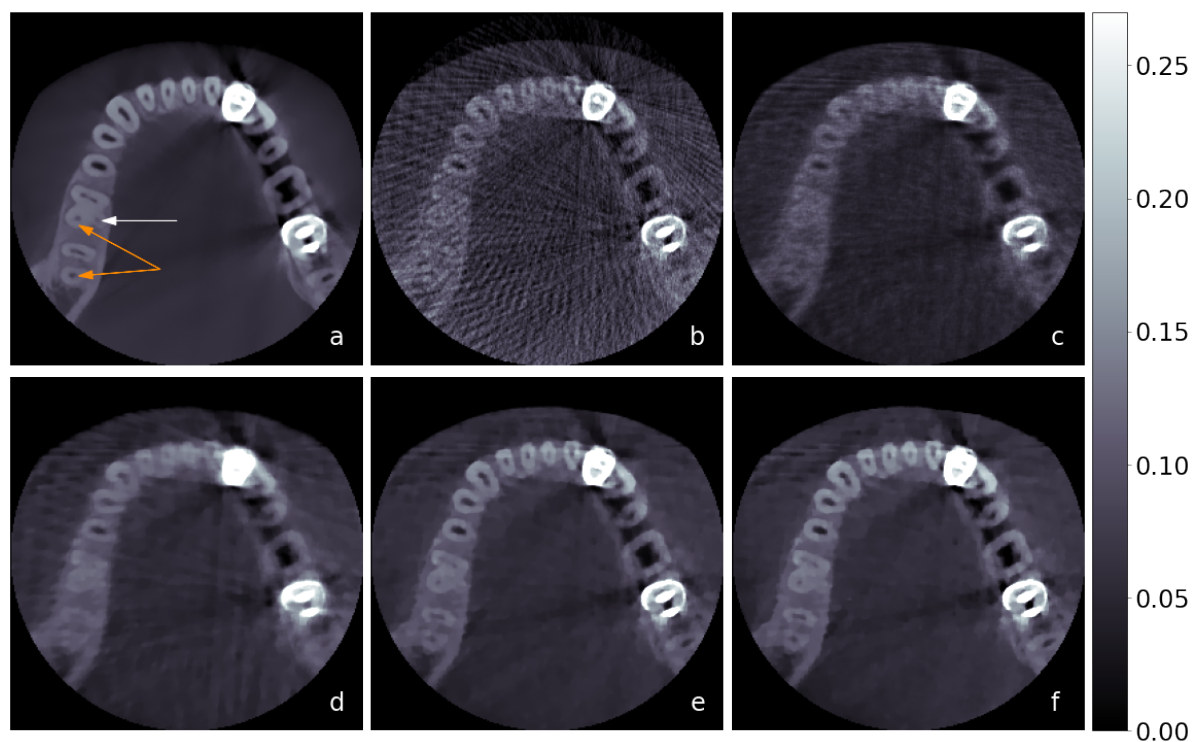


Figure 10. Axial slice containing metal of the dental reconstruction, in ultra low-dose. (a) Ground truth, (b) FDK, (c) MLEM, (d) SIRT-TV, (e) MLEM-TV, (f) KL-TV. The orange arrows point to root canals erased in MLEM and SIRT-TV reconstruction, and the white one to a canal not reconstructed with any method.

A zoom on the mandibular left first molar already shown in low dose in figure 8 can be seen in figure 11. The mandibular canal (light-blue arrow) is visible in the three TV reconstructions. FDK and MLEM gave images where details are lost. The root canal (blue arrow) in the SIRT-TV reconstruction is not visible enough and the pulp chamber (pink arrow) is shrunk. MLEM-TV and KL-TV algorithms reconstruct the most accurate volume, although some details are lost in particular for bone trabeculae.

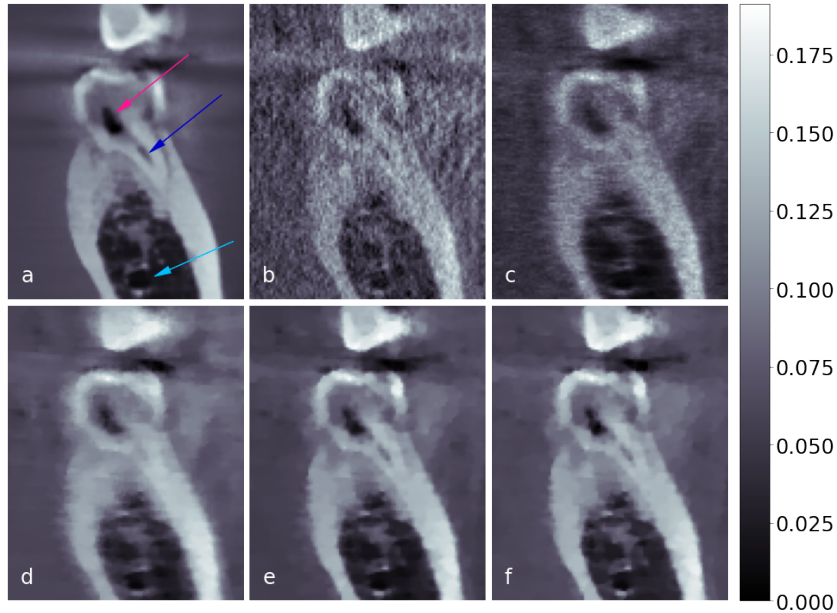


Figure 11. Zoom on a tooth in a coronal slice, in ultra low-dose. (a) Ground truth, (b) FDK, (c) MLEM, (d) SIRT-TV, (e) MLEM-TV (f) KL-TV. Pink, blue and light-blue arrows indicate respectively the pulp chamber, the root canal and the mandibular canal.

Reconstructions including regularization clearly outperformed analytical and MLEM reconstructions. Although for the phantom SIRT-TV was comparable with MLEM-TV and KL-TV, in the reconstruction of experimental data the results are blurred and lack contrast. MLEM-TV and KL-TV reconstructions are very similar, with a mutual correlation of over 0.99 in both dose configurations.

The reconstruction times are shown in table 6. As in the phantom reconstruction, the algorithms using TV regularization are more time consuming than MLEM. The computation times are roughly equivalent for the other three methods in both dose configuration with an advantage for KL-TV. Ranking in terms of speed differs between low-dose and ultra low-dose. This difference comes from the fact that the algorithms do not have the same architecture, so the time complexity with respect to the projections size is different for each of them. We conjecture that the computing time is influenced by memory management procedures and might be improved by adequate implementation.

	FDK	MLEM (400)	SIRT-TV (400-20)	MLEM-TV (400-20)	KL-TV (700)
Low-dose	00:00:06	00:30:00	01:15:40	01:08:40	00:58:55
Ultra low-dose	00:00:03	00:27:20	00:54:40	01:05:44	00:55:25

Table 6. Reconstruction times of the experimental data for the different algorithms.

5. Discussion

Our results for both simulated and experimental data clearly demonstrate that a significant improvement of image quality can be obtained when regularized models are considered in conjunction with iterative reconstructions. We compared three such algorithms: SIRT-TV, KL-TV and MLEM-TV. While typically classified as an algebraic method, SIRT can also be considered as an EM algorithm maximizing the likelihood for Gaussian data [Yan et al., 2011]. Equivalently, this corresponds to the minimization of a quadratic data fidelity term. KL-TV and MLEM-TV both use the Kullback-Leibler distance in the definition of the data fidelity term. Note that minimizing the Kullback-Leibler distance is equivalent to maximize the Poisson likelihood function [Titterington, 1987]. The Poisson distribution seems better suited to model low-dose data compared to Gaussian distribution, although a more complete model could also account for Gaussian uncertainties at detection. Tests made in 2D with parallel projections which were not shown here suggest that when the Poisson noise is predominant, the algorithms based on the KL distance outperform SIRT-TV while the opposite holds when Gaussian noise is predominant. Our tests have shown better performances for the KL-TV and MLEM-TV algorithms for our experimental data, which supports the need to include Poisson noise when modeling low-dose CBCT.

Although a positive bias is present in zero-valued regions of the MLEM reconstruction, no bias was observed in the experimental data reconstruction. Efficient streak artifact reduction was observed with regularized iterative methods. Enhanced by the presence of metal, those artifacts are especially visible in the standard FDK reconstruction. Iterative methods reduce them although they remain visible in the low frequencies and cannot be eliminated by an increase in the TV parameter without a significant loss of the details in the images. These artifacts could be further attenuated with a metal artifact reduction algorithm.

Table 7 summarizes the algorithms used in this study, with their principal strengths and weaknesses.

	Method	Functional	Speed	Artifact reduction	Noise reduction	Detail restoration
FDK	Analytic	None	++	None	-	++
MLEM	Likelihood	$KL(Af, p)$	+	+	-	-
SIRT-TV	MAP-EM	$\frac{1}{2}\ Af - p\ _2^2 + \alpha TV(f)$	--	++	+	+
MLEM-TV	MAP-EM	$KL(Af, p) + \alpha TV(f)$	--	+++	+	++
KL-TV	PDHG	$KL(Af, p) + \alpha TV(f)$	-	+++	+	++

Table 7. Summary of the five algorithms. We recall the methods on which they are based, the functional to minimize, reconstruction time, artifact reduction capabilities, noise reduction and detail restoration.

In dental CBCT, the distribution of the dose is not uniform through the volume since more dose is given to central region where the region of interest is located. The

mathematical transcription of the received dose is the sensitivity, defined in equation (9). Higher values of the sensitivity are observed at the region of interest and lower values near the boundaries. Moreover, in dental CBCT, an extension of the volume is necessary because of the truncated projections and leads to even more important discrepancies. This leads to an inhomogeneity in the mathematical projection model not encountered in parallel beam models that has two important consequences on the two regularized statistical methods. One of them is related to the convergence of the KL-TV and MLEM-TV algorithms. For KL-TV we implemented the preconditioned version of the PDHG algorithm from [Pock and Chambolle, 2011]. For MLEM-TV we introduced in this work a preconditioned version of the algorithm that prevents numerical divergence when the minimum of the sensitivity is small. The other consequence concerns the convergence speed and preconditioning allows to improve it for both algorithms. For the original MLEM-TV, the convergence of the TV denoising stage depends on the gradient step τ in (25), which decreases with the minimum of the sensibility s_{min} . With preconditioning we allow this step to vary with the sensitivity, which thus has a faster convergence when denoising the central part of the volume, the one corresponding to the FOV.

To sum up, inhomogeneities in the projection model along with ill-conditioning resulting from projection truncation lead to some challenges, which we were able to overcome by implementing tailored numerical optimization schemes. Not much studies address these issues. We can cite for instance [Stsepankou et al., 2012], where a Poisson data distribution and TV regularization are considered for low-dose CBCT data. The reconstruction is carried out with the MAP-TV algorithm from [Green, 1990]. However this algorithm is not stable even if numerical convergence can be obtained for small regularization parameters. The upper limit of regularization parameter depends on the minimum of the sensitivity as for MLEM-TV. However in their work, some of the issues we face are circumvented as the experimental data set is composed of complete projections from image-guided radiation therapy.

In terms of computation time, depending on the configuration, MLEM-TV is either comparable or slower than KL-TV. The difference between the two is that KL-TV requires more projection and back-projection operations where MAP-TV performs a full TV denoising at each iteration. These conclusions are different from what was shown in a previous work [Leuliet et al., 2021] on 2D reconstructions from parallel projections and on 3D experimental electron microscopy data. This is related once again to the non-uniformity of the sensitivity across the volume. The major part of the computation time in MLEM-TV was spent in the denoising steps. This part was implemented on GPU using the library Cupy from Python. It is likely that some acceleration may be obtained with a more adequate implementation, making TV and reconstruction steps comparable. Using OSEM instead of MLEM could also lead to some acceleration.

The value of the TV parameter influences the denoising quality and the accuracy of the reconstruction. If the parameter is too large, details of the image will be removed, while if it is too small, one will not denoise enough. Hence, the choice of this parameter is decisive for the quality of the reconstruction. A rich literature exists on methods capable

to automatically compute the optimal parameter. They are based on the discrepancy principle or on risk estimators. We tried the rule presented in [Ito et al., 2011], where the authors define the regularization parameter by minimizing a functional based on the cost function used in the reconstruction algorithm. If this method had given good results in 2D parallel geometry, in our case, the obtained value was unstable. It has been shown in [Lucka et al., 2018] that automatic methods are not necessarily adapted for severely ill-posed problems. However, we observed in our experiments that with a rather similar configuration (same dose, number of projections, presence of metal or not), the same TV parameter could be kept for all volumes. Thus, it would be possible to determine a fixed number of configurations with their associated parameters.

Iterative methods have some limits. Even if the use of graphics processing units allows to accelerate the iterative 3D reconstructions, they remain rather slow for application in clinical environment and require large memory resources. The TV regularization we applied in this work is largely accepted as a state-of-the-art method. However TV is known to favor piecewise constant areas and produce a "cartoon" effect in the image. Some small structures may be removed and the texture is modified.

6. Conclusion

The main purpose of this work was the evaluation of 3D CBCT reconstruction methods by means of iterative schemes and TV regularization in dental imaging. The numerical schemes were adapted to the cone-beam geometry and the truncated nature of the projections. We successfully applied four iterative algorithms to 3D phantom and experimental dental data. The test we carried on an ultra low-dose projections set allowed to evaluate the algorithms in a quite extreme situation. The TV regularization clearly improves the quality of the reconstruction. The KL-TV and MLEM-TV algorithms gave the best reconstructions in terms of computation time and reconstruction accuracy.

Compared to standard FDK reconstruction, iterative methods have demonstrated improvements in image quality in reconstruction of low-dose CT data acquired with increased photonic noise due to the lower X-ray tube current. In this study, we choose to investigate situations where the dose is lowered by reducing the number of acquired projections. With a single acquisition, the normal and the low dose can be obtained simultaneously by subsampling the first one in order to obtain the second. This way, the low dose image can be compared to the reference obtained in normal dose. Previous work on other low-dose applications has demonstrated that lowering the current is more advantageous compared to reducing the number of projections [Zhao et al., 2014]. Our objective was to investigate the algorithms on experimental data, while still having a reference image of the object. Tests on acquisitions with lower current will be addressed in the future.

Even if the computation times are currently quite large, optimization of the implementation of the algorithms, parallel computing and additional hardware

acceleration may lower reconstructions times to the point they become acceptable for clinical practice. Moreover, these methods have the ability to use the knowledge of the acquisition geometry as well as exact projection and backprojection operations.

Data-driven methods are an interesting perspective since, once trained, they are expected to provide good quality reconstructions in a few seconds. Nevertheless Deep Learning methods require a large amount of data for training. This is a critical issue in medical imaging, since it may be difficult to obtain a sufficient number of low-dose/high-dose image pairs to train DL networks, especially on patients. Thus, the iterative reconstruction algorithms developed in this work applied to low-dose projections could be used as a surrogate to high-dose images for training DL networks.

Acknowledgements

This work was performed within the framework of the LABEX PRIMES (ANR-11-LABX-0063) of Université de Lyon, within the program “Investissements d’Avenir” (ANR-11-IDEX-0007). We acknowledge CARESTREAM Dental for providing us the experimental data.

Bibliography

- [Adler and Öktem, 2018] Adler, J. and Öktem, O. (2018). Learned primal-dual reconstruction. *IEEE transactions on medical imaging*, 37(6):1322–1332.
- [Andersen and Kak, 1984] Andersen, A. H. and Kak, A. C. (1984). Simultaneous algebraic reconstruction technique (SART): a superior implementation of the ART algorithm. *Ultrasonic imaging*, 6(1):81–94.
- [Anthoine et al., 2012] Anthoine, S., Aujol, J.-F., Boursier, Y., and Melot, C. (2012). Some proximal methods for Poisson intensity CBCT and PET. *Inverse Problems & Imaging*, 6(4):565–598.
- [Aootaphao et al., 2021] Aootaphao, S., Thongvigitmanee, S., Puttawibul, P., and Thajchayapong, P. (2021). Truncation effect reduction for fast iterative reconstruction in cone-beam CT.
- [Baba et al., 2004] Baba, R., Ueda, K., and Okabe, M. (2004). Using a flat-panel detector in high resolution cone beam CT for dental imaging. *Dentomaxillofacial radiology*, 33(5):285–290.
- [Banjak, 2016] Banjak, H. (2016). *X-ray Computed Tomography Reconstruction on Non-Standard Trajectories for Robotized Inspection*. PhD thesis, INSA Lyon.
- [Banjak et al., 2018] Banjak, H., Grenier, T., Epicier, T., Koneti, S., Roiban, L., Gay, A.-S., Magnin, I., Peyrin, F., and Maxim, V. (2018). Evaluation of noise and blur effects with SIRT-FISTA-TV reconstruction algorithm: Application to fast environmental transmission electron tomography. *Ultramicroscopy*, 189:109–123.
- [Bayaraa et al., 2020] Bayaraa, T., Hyun, C. M., Jang, T. J., Lee, S. M., and Seo, J. K. (2020). A two-stage approach for beam hardening artifact reduction in low-dose dental CBCT. *IEEE Access*, 8:225981–225994.
- [Beck and Teboulle, 2009a] Beck, A. and Teboulle, M. (2009a). Fast gradient-based algorithms for constrained total variation image denoising and deblurring problems. *IEEE transactions on image processing*, 18(11):2419–2434.
- [Beck and Teboulle, 2009b] Beck, A. and Teboulle, M. (2009b). A fast iterative shrinkage-thresholding algorithm for linear inverse problems. *SIAM journal on imaging sciences*, 2(1):183–202.
- [Chambolle, 2004] Chambolle, A. (2004). An algorithm for total variation minimization and applications. *Journal of Mathematical imaging and vision*, 20(1-2):89–97.

- [Chambolle and Pock, 2011] Chambolle, A. and Pock, T. (2011). A first-order primal-dual algorithm for convex problems with applications to imaging. Journal of mathematical imaging and vision, 40(1):120–145.
- [Chen et al., 2015] Chen, G., Zhu, F., and Ann Heng, P. (2015). An efficient statistical method for image noise level estimation. In Proceedings of the IEEE International Conference on Computer Vision, pages 477–485.
- [Dang et al., 2016] Dang, H., Stayman, J. W., Sisniega, A., Zbijewski, W., Xu, J., Wang, X., Foos, D. H., Aygun, N., Koliatsos, V. E., and Siewerdsen, J. H. (2016). Multi-resolution statistical image reconstruction for mitigation of truncation effects: application to cone-beam CT of the head. Physics in Medicine & Biology, 62(2):539.
- [Dempster et al., 1977] Dempster, A. P., Laird, N. M., and Rubin, D. B. (1977). Maximum likelihood from incomplete data via the EM algorithm. Journal of the Royal Statistical Society: Series B (Methodological), 39(1):1–22.
- [Feldkamp et al., 1984] Feldkamp, L. A., Davis, L. C., and Kress, J. W. (1984). Practical cone-beam algorithm. Josa a, 1(6):612–619.
- [Gilbert, 1972] Gilbert, P. (1972). Iterative methods for the three-dimensional reconstruction of an object from projections. Journal of theoretical biology, 36(1):105–117.
- [Gordon et al., 1970] Gordon, R., Bender, R., and Herman, G. T. (1970). Algebraic reconstruction techniques (ART) for three-dimensional electron microscopy and X-ray photography. Journal of theoretical Biology, 29(3):471–481.
- [Green, 1990] Green, P. J. (1990). Bayesian reconstructions from emission tomography data using a modified EM algorithm. IEEE Transactions on Medical Imaging, 9(1):84–93.
- [Hsieh et al., 2004] Hsieh, J., Chao, E., Thibault, J., Grekowitz, B., Horst, A., McOlash, S., and Myers, T. (2004). A novel reconstruction algorithm to extend the CT scan field-of-view. Medical physics, 31(9):2385–2391.
- [Hudson and Larkin, 1994] Hudson, H. and Larkin, R. (1994). Accelerated image reconstruction using ordered subsets of projection data. IEEE Transactions on Medical Imaging, 13(4):601–609.
- [Humphries et al., 2019] Humphries, T., Si, D., Coulter, S., Simms, M., and Xing, R. (2019). Comparison of deep learning approaches to low dose CT using low intensity and sparse view data. In Medical Imaging 2019: Physics of Medical Imaging, volume 10948, pages 1048–1054. SPIE.
- [Ibraheem et al., 2012] Ibraheem, I. et al. (2012). Reduction of artifacts in dental cone beam CT images to improve the three dimensional image reconstruction. J Biomed Sci Eng, 5(8):409–15.
- [Ito et al., 2011] Ito, K., Jin, B., and Takeuchi, T. (2011). A regularization parameter for nonsmooth Tikhonov regularization. SIAM Journal on Scientific Computing, 33(3):1415–1438.
- [Jin et al., 2017] Jin, K. H., McCann, M. T., Froustey, E., and Unser, M. (2017). Deep convolutional neural network for inverse problems in imaging. IEEE Transactions on Image Processing, 26(9):4509–4522.
- [Kaasalainen et al., 2021] Kaasalainen, T., Ekholm, M., Siiskonen, T., and Kortensniemi, M. (2021). Dental cone beam CT: An updated review. Physica Medica, 88:193–217.
- [Kolehmainen et al., 2003] Kolehmainen, V., Siltanen, S., Järvenpää, S., Kaipio, J. P., Koistinen, P., Lassas, M., Pirttilä, J., and Somersalo, E. (2003). Statistical inversion for medical x-ray tomography with few radiographs: II. Application to dental radiology. Physics in Medicine & Biology, 48(10):1465.
- [Lange et al., 1984] Lange, K., Carson, R., et al. (1984). EM reconstruction algorithms for emission and transmission tomography. J Comput Assist Tomogr, 8(2):306–16.
- [Leuliet et al., 2021] Leuliet, T., Friot--Giroux, L., Baaziz, W., Bretin, É., Ersen, O., Peyrin, F., Sixou, B., and Maxim, V. (2021). Efficiency of TV-regularized algorithms in computed tomography with Poisson-Gaussian noise. In 2020 28th European Signal Processing Conference (EUSIPCO), pages 1294–1298. IEEE.
- [Leuschner et al., 2021] Leuschner, J., Schmidt, M., Baguer, D. O., and Maass, P. (2021). LoDoPaB-

- CT, a benchmark dataset for low-dose computed tomography reconstruction. Scientific Data, 8(1):1–12.
- [Li et al., 2019] Li, Y., Li, K., Zhang, C., Montoya, J., and Chen, G.-H. (2019). Learning to reconstruct computed tomography images directly from sinogram data under a variety of data acquisition conditions. IEEE transactions on medical imaging, 38(10):2469–2481.
- [Liang et al., 2010] Liang, X., Lambrechts, I., Sun, Y., Denis, K., Hassan, B., Li, L., Pauwels, R., and Jacobs, R. (2010). A comparative evaluation of cone beam computed tomography (CBCT) and multi-slice CT (MSCT). Part II: On 3D model accuracy. European journal of radiology, 75(2):270–274.
- [Liu et al., 2015] Liu, Y., Shangguan, H., Zhang, Q., Zhu, H., Shu, H., and Gui, Z. (2015). Median prior constrained TV algorithm for sparse view low-dose CT reconstruction. Computers in biology and medicine, 60:117–131.
- [Lucka et al., 2018] Lucka, F., Proksch, T., Brune, C., Bissantz, N., Burger, M., Dette, H., and Wubbeeling, F. (2018). Risk estimators for choosing regularization parameters in ill-posed problems-properties and limitations. Inverse Problems and Imaging, 12(5):1121–1155.
- [Maltz et al., 2007] Maltz, J. S., Bose, S., Shukla, H. P., and Bani-Hashemi, A. R. (2007). CT truncation artifact removal using water-equivalent thicknesses derived from truncated projection data. In 2007 29th annual international conference of the IEEE engineering in medicine and biology society, pages 2907–2911. IEEE.
- [Maxim et al., 2018] Maxim, V., Feng, Y., Banjak, H., and Bretin, E. (2018). Tomographic reconstruction from Poisson distributed data: a fast and convergent EM-TV dual approach. preprint, INSA Lyon, <https://hal.archives-ouvertes.fr/hal-01892281/>.
- [Mtanglos et al., 1995] Mtanglos, S. H., Gagne, G. M., Krol, A., Thomas, F. D., and Narayanaswamy, R. (1995). Transmission maximum-likelihood reconstruction with ordered subsets for cone beam CT. Physics in Medicine & Biology, 40(7):1225.
- [Ohnesorge et al., 2000] Ohnesorge, B., Flohr, T., Schwarz, K., Heiken, J., and Bae, K. (2000). Efficient correction for CT image artifacts caused by objects extending outside the scan field of view. Medical physics, 27(1):39–46.
- [Panin et al., 1999] Panin, V. Y., Zeng, G. L., and Gullberg, G. T. (1999). Total variation regulated EM algorithm. IEEE Transactions on Nuclear Science, 46(6):2202–2210.
- [Park and Ye, 2020] Park, S. and Ye, J. C. (2020). Unsupervised Cone-Beam artifact removal using CycleGAN and spectral blending for adaptive radiotherapy. ISBI.
- [Persson et al., 2001] Persson, M., Bone, D., and Elmqvist, H. (2001). Total variation norm for three-dimensional iterative reconstruction in limited view angle tomography. Physics in Medicine & Biology, 46(3):853.
- [Pock and Chambolle, 2011] Pock, T. and Chambolle, A. (2011). Diagonal preconditioning for first order primal-dual algorithms in convex optimization. In 2011 International Conference on Computer Vision, pages 1762–1769.
- [Rudin et al., 1992] Rudin, L. I., Osher, S., and Fatemi, E. (1992). Nonlinear total variation based noise removal algorithms. Physica D: nonlinear phenomena, 60(1-4):259–268.
- [Sawatzky et al., 2008] Sawatzky, A., Brune, C., Wubbeeling, F., Kusters, T., Schafers, K., and Burger, M. (2008). Accurate EM-TV algorithm in PET with low SNR. In 2008 IEEE nuclear science symposium conference record, pages 5133–5137. IEEE.
- [Shepp and Vardi, 1982] Shepp, L. and Vardi, Y. (1982). Maximum likelihood reconstruction for emission tomography. IEEE Transactions on Medical Imaging, 1(2):113–122.
- [Sidky et al., 2012] Sidky, E. Y., Jørgensen, J. H., and Pan, X. (2012). Convex optimization problem prototyping for image reconstruction in computed tomography with the Chambolle-Pock algorithm. Physics in Medicine & Biology, 57(10):3065.
- [Sidky et al., 2006] Sidky, E. Y., Kao, C.-M., and Pan, X. (2006). Accurate image reconstruction from few-views and limited-angle data in divergent-beam CT. Journal of X-ray Science and Technology, 14(2):119–139.

- [Stsepankou et al., 2012] Stsepankou, D., Arns, A., Ng, S., Zygmanski, P., and Hesser, J. (2012). Evaluation of robustness of maximum likelihood cone-beam CT reconstruction with total variation regularization. *Physics in Medicine & Biology*, 57(19):5955.
- [Titterington, 1987] Titterington, D. (1987). On the iterative image space reconstruction algorithm for ECT. *IEEE transactions on medical imaging*, 6(1):52–56.
- [Van Aarle et al., 2016] Van Aarle, W., Palenstijn, W. J., Cant, J., Janssens, E., Bleichrodt, F., Dabravolski, A., De Beenhouwer, J., Batenburg, K. J., and Sijbers, J. (2016). Fast and flexible X-ray tomography using the ASTRA toolbox. *Optics express*, 24(22):25129–25147.
- [Vardi et al., 1985] Vardi, Y., Shepp, L., and Kaufman, L. (1985). A statistical model for positron emission tomography. *Journal of the American Statistical Association*, 80(389):8–20.
- [Widmann and Asma’a, 2018] Widmann, G. and Asma’a, A. (2018). Suppl-1, M5: Ultralow Dose MSCT Imaging in Dental Implantology. *The open dentistry journal*, 12:87.
- [Widmann et al., 2017] Widmann, G., Bischel, A., Stratis, A., Bosmans, H., Jacobs, R., Gassner, E.-M., Puelacher, W., and Pauwels, R. (2017). Spatial and contrast resolution of ultralow dose dentomaxillofacial CT imaging using iterative reconstruction technology. *Dentomaxillofacial Radiology*, 46(4):20160452.
- [Yan et al., 2011] Yan, M., Chen, J., Vese, L. A., Villasenor, J., Bui, A., and Cong, J. (2011). EM+TV Based Reconstruction for Cone-Beam CT with Reduced Radiation. In *Advances in Visual Computing*, pages 1–10. Springer Berlin Heidelberg.
- [Yu et al., 2012] Yu, L., Shiung, M., Jondal, D., and McCollough, C. H. (2012). Development and validation of a practical lower-dose-simulation tool for optimizing computed tomography scan protocols. *Journal of computer assisted tomography*, 36(4):477–487.
- [Zhao et al., 2014] Zhao, Z., Gang, G., and Siewerdsen, J. (2014). Noise, sampling, and the number of projections in cone-beam CT with a flat-panel detector. *Medical Physics*, 41(6Part1):061909.